Nano Research

ISSN 1998-0124 CN 11-5974/O4
https://doi.org/10.1007/s12274-022-4768-6

Research Article

In-situ construction of a thermodynamically stabilized interface on the surface of single crystalline Ni-rich cathode materials via a one-step molten-salt route

Huiya Yang, Xiangbang Kong, Jiyang Li, Pengpeng Dai, Jing Zeng, Yang Yang (✉), and Jinbao Zhao (✉)

State Key Laboratory of Physical Chemistry of Solid Surfaces, Collaborative Innovation Centre of Chemistry for Energy Materials, State-Province Joint Engineering Laboratory of Power Source Technology for New Energy Vehicle, Engineering Research Center of Electrochemical Technology, Ministry of Education, College of Chemistry and Chemical Engineering, Xiamen University, Xiamen 361005, China

Received: 10 May 2022 / **Revised:** 15 June 2022 / **Accepted:** 13 July 2022

ABSTRACT

Nickel rich $LiNi_xCo_yMn_{1-x-y}O_2$ cathode materials have been studied extensively to increase the energy density of lithium-ion batteries (LIBs) due to their advantages of high capacity and low cost. However, the anisotropic crystal expansion and contraction inside the secondary particles would cause detrimental micro-cracks and severe parasitic reactions at the electrode/electrolyte interface during cycling, which severely decreases the stability of crystalline structure and cathode-electrolyte interphase and ultimately affects the calendar life of batteries. Herein, a thermodynamically stabilized interface is constructed on the surface of single-crystalline Ni-rich cathode materials (SC811@RS) via a facile molten-salt route to suppress the generation of microcracks and interfacial parasitic side reactions simultaneously. Density functional theory calculations show that the formation energy of interface layer (−1.958 eV) is more negative than that of bulk layered structure (−1.421 eV). Such a thermodynamically stable protective layer can not only prevent the direct contact between highly reactive $LiNi_xCo_yMn_{1-x-y}O_2$ and electrolyte, but also mitigate deformation of structure caused by stress thus strengthening the mechanical properties. Raman spectra further confirm the excellent structural reversibility and reaction homogeneity of SC811@RS at particle, electrode, and time scales. Consequently, SC811@RS cathode material delivers significantly improved cycling stability (high capacity retention of 92% after 200 cycles at 0.5 C) compared with polycrystalline $LiNi_{0.8}Co_{0.1}Mn_{0.1}O_2$ (82%).

KEYWORDS

$LiNi_xCo_yMn_{1-x-y}O_2$, single crystalline, polycrystalline, cathode, lithium-ion battery

1 Introduction

Since the commercialization in 1991, lithium-ion batteries (LIBs) have been widely applied to various portable electric vehicles and electronic devices [1–3]. However, as for their application in electric vehicles, the limitation of driving range is still a primary concern among customers, which puts forward a higher requirement for their energy densities [4–6]. Considering the specific capacity of cathode materials is much lower than that of anode materials, which has become a decisive factor for the energy density of LIBs [3, 7]. Among the various cathode materials, ternary Ni-Co-Mn (NCM) materials are regarded as one of the next-generation cathode materials for high energy LIBs, benefiting from their intrinsic high capacity and low cost [4]. However, the NCM cathode materials still face the challenge of unsatisfactory cycling stability [8–11].

The most widely used NCM cathode materials are polycrystalline, which are actually micro-sized secondary particles composed of smaller primary particles. Therefore, the intergranular cracks would inevitably appear among the grain boundaries due to the anisotropic stress and volume change caused by the randomly orientated primary particles during the charge and discharge processes. These irreversible intergranular cracks block the electron transmission, resulting in the capacity decay of polycrystalline materials. Moreover, the delithiated NCM cathode materials is thermodynamically unstable. The electrolyte also penetrates into the bulk region of secondary particles along the cracks, which enlarges the contact interface areas between electrode materials and electrolyte, aggravating the interface parasitic reactions [12, 13]. And such a negative effect is much more severe with the increased nickel content in NCM materials. The accumulation of side reactions induces the phase transformation and the dissolution of transition metal ions, leading to the decrease of structural stability and thermal stability. To mitigate these above problems, various modification strategies including doping, surface coating, and concentration gradient construction have been extensively studied, but the key point of micro-cracks is still hard to be solved fundamentally [14–20].

Single-crystallization is an effective way to alleviate the generation of cracks. The single crystalline particles without grain boundaries in their inherent structure eliminate the formation of cracks and reduce the parasitic reactions [21]. At the same time, a high-pressure compact density electrode can be obtained due to the high strength of single crystalline particles. So far, some single crystalline NCM electrode materials have been synthesized as

Address correspondence to Yang Yang, yangyang419@xmu.edu.cn; Jinbao Zhao, jbzhao@xmu.edu.cn

reported. Single crystalline $LiNi_{0.5}Co_{0.2}Mn_{0.3}O_2$ was synthesized at a high calcination temperature of 970 °C [22]. The increase of calcination temperature can promote the formation of single crystalline morphology, because the ion mobility and the rate of grain growth increase as the temperature rises. However, higher calcination temperature promotes severe agglomeration and it is difficult to obtain dispersed primary particles directly. Subsequent operations such as grinding and crushing are used to disperse the agglomerated particles, which leads to the damage of morphology and the formation of surface defects. Another method for the fabrication of single crystalline materials is molten-salt synthesis [23]. In this method, one or more salts with the low melting point are added into the precursor, so a liquid environment can be formed when the mixture is heated to a relatively low temperature. This can promote the dissolution and diffusion of species and provide an additional way for the crystal growth. Using NaCl and KCl salts for the molten-salt synthesis of $LiNi_{0.8}Co_{0.1}Mn_{0.1}O_2$ (NCM811), Kim et al. obtained the single crystalline particles with an almost perfect octahedral figure [24]. In this case, it is difficult to obtain single crystalline particles with uniform size when the calcining temperature is lower. However, when the calcining temperature reaches 1,000 °C, the Li/Ni cation mixing proportion of nickel-rich cathode materials increased seriously, which damages the electrochemical performance of cathode materials. In addition, sodium and potassium ions may be doped into NCM structures causing changes of structure.

Hence, the uniform single crystalline NCM811 (SC811) particles are prepared at lower temperature via $LiOH/Li_2SO_4$ molten salt in this work. The evolution mechanism of single crystalline particles is inferred by observing the morphology of primary particles under different conditions, which has not been reported and systematically investigated before. In addition, the thermodynamically stabilized interface of SC811 is also *in-situ* constructed during the preparation process (the material named SC811@RS). As reported in the literature, the combination of thermodynamically stabilized interface and layered structure would enable cathode materials to exert a better performance [25–27]. Moreover, the cycle stability of the SC811 materials has been significantly improved compared with the polycrystalline NCM811 (PC811) materials. The main cause for the capacity improvement of SC811@RS can be attributed to the crack-free structure of material and the restraint of the bulk and surface structural deterioration of materials as well as the reaction homogeneity at the particle and electrode scale (Fig. 1). This research can help guide the synthesis of superior single crystalline NCM cathode materials, deeply understand the performance degradation mechanism, and promote the large-scale application of single crystalline NCM materials.

2 Experimental section

2.1 Synthesis of SC811@RS material

The $Ni_{0.8}Co_{0.1}Mn_{0.1}(OH)_2$ precursor was provided by Beijing Easpring Material Technology Co., Ltd. (China). The $Ni_{0.8}Co_{0.1}Mn_{0.1}(OH)_2$ precursor was mixed with Li_2SO_4 (AR, Aladdin) and LiOH (AR, Aladdin) thoroughly at a mole ratio of 4:1:4.4/5.2/6.0/6.8/7.6, in which the relative amount of LiOH was changed. The excess lithium salt could not only provide the molten-salt environment for the single crystalline growth but also compensate for the lithium loss in sintering process. The mixture of precursor and salts was preheated at 500 °C for 3 h and calcined in an oxygen atmosphere at 700/800/850/900/920 °C for 0/5/10 h with a heating rate of 5 °C·min^{-1}. For comparison, the $Ni_{0.8}Co_{0.1}Mn_{0.1}(OH)_2$ precursor and LiOH (5% excess) were calcined at 750 °C for 15 h to obtain the PC811 material.

2.2 Electrochemical measurements

The cathode electrode was fabricated with 80 wt.% SC811@RS, 10 wt.% polyvinylidene fluoride (PVDF) in N-methy-1,2-pyrrolidone (NMP), and 10 wt.% super P. The SC811@RS electrode, the Li metal counter electrode, the electrolyte (1 M

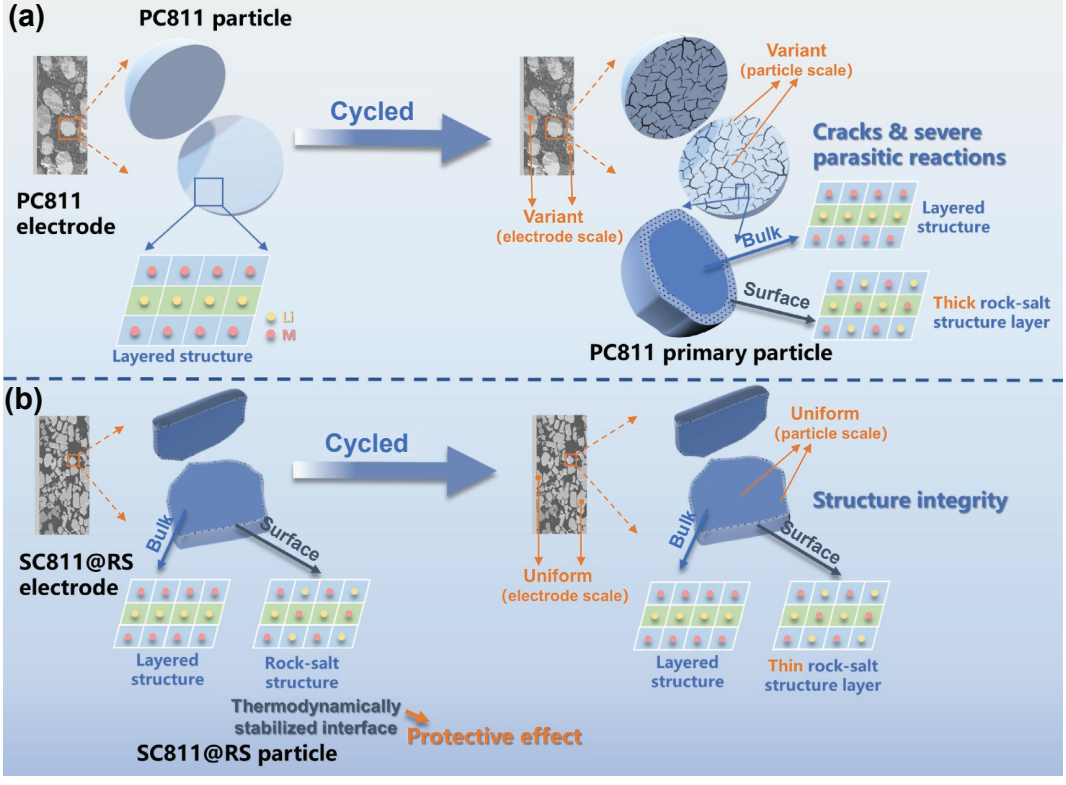

Figure 1 Schematic diagram of cyclic performance deterioration mechanism.

$LiPF_6$ in the EC-DMC solvent, EC:DMC = 1:1 v/v), and the polyethylene porous separator were assembled into half-cells in an Ar-filled glove box. Electrochemical property tests were performed on the LAND battery testing system at 25 °C. The electrochemical impedance spectroscopy (EIS) measurement was tested by electrochemical workstation (Solartron 1287/1260).

2.3 Simulation method

All the density functional theory (DFT) calculations were conducted with the Vienna *ab initio* simulation package (VASP) [28]. The generalized gradient approximation (GGA) and Perdew–Burke–Ernzerhof (PBE) formulation were adopted to describe the exchange correlation energies [29, 30]. The projector augmented wave (PAW) method was used to describe the ionic cores [31, 32], and valence electrons were considered using a plane wave basis with a kinetic energy cutoff of 450 eV. Partial occupancies of the Kohn–Sham orbitals were allowed using the Gaussian smearing method with a width of 0.05 eV. The electronic energy was considered self-consistent when the energy change was smaller than 10^{-4} eV. The convergence criterion of geometry relaxation was smaller than 0.03 eV·Å^{-1}. The Brillouin zones (BZ) were sampled by using the surfaces structures of 2 × 2 × 2 Monkhorst–Pack *K* point. In our structure, the Li-Ni atoms had been mixed with each other randomly to construct rock-salt structures. Finally, we defined the formation energy per atom (E_f) of a compound

$$E_f = E_{total} - N_{Li}\mu_{Li} - N_{Ni}\mu_{Ni} - N_O\mu_O \quad (1)$$

where E_{total} is the total DFT energy of a given structure, μ_{Li}, μ_{Ni}, and μ_O are the chemical potentials of the constituent atomic species, and N_{Li}, N_{Ni}, and N_O are the number of the constituent atomic species. To calculate the stress on structures, the lattice constant *c* was fixed at each specific value, and other lattice constants (*a* and *b*) were relaxed during the structural optimization. For the strained structures, the strain could be defined as the ratio between the change of lattice constant (Δc) and the optimized lattice constant (*c*).

2.4 Structural characterization

The inductively coupled plasma atomic emission spectroscopy (ICP-AES) Plasma 1000 (NCS, China) was used to identify the chemical composition of SC81. The scanning electron microscopy (SEM, Zeiss GeminiSEM 500) equipped with an energy dispersive spectrometer (EDS) was used to characterize the morphology of samples. The microstructure changes before and after cycling were observed through transmission electron microscopy (TEM, FEI Tecnai F30). The crystal structure of samples was identified by X-ray diffraction (XRD, Rigaku Miniflex 600) with a scan rate of 2 °·min^{-1} and Cu Kα radiation, and the recorded data was analyzed by General Structure Analysis System Rietveld (GSAS) refinement software. X-ray photoelectron spectroscopy (XPS, Thermo Scientific ESCALAB Xi+) was used to analyze the surface element of material. Raman spectroscopy (Horiba LabRAM HR Evolution) was used to characterize the structural evolution of cathode materials, with a 532 nm wavelength of laser and a 0.28 mW power.

3 Results and discussion

3.1 Synthesis, characterization, and electrochemical performance of SC811@RS particles

The optimal synthesis conditions of SC811@RS cathode materials are scientifically explored. In Fig. S1 in the Electronic Supplementary Material (ESM), by comparing the morphology and XRD results of synthesized materials in different molten-salt systems (NaCl-LiOH, LiCl-LiOH, $LiNO_3$-LiOH, and Li_2SO_4-LiOH), it is confirmed that the LiOH-Li_2SO_4 eutectic-salt system is most appropriate. Combining the phase diagram analysis with differential scanning calorimetry (DSC) (Fig. S2 in the ESM), a synthetic route (Fig. S3 in the ESM) to prepare single crystalline materials is designed, in which the molar ratio of $Ni_{0.8}Co_{0.1}Mn_{0.1}(OH)_2$:$Li_2SO_4$:LiOH is set as 4:1:4.4/5.2/6.0/6.8/7.6 respectively (Table S1 in the ESM) and preheat temperature is 500 °C [33]. As indicated by the SEM and XRD profiles (Figs. S4 and S5, and Table S2 in the ESM) of NCM811 synthesized at different calcination temperatures with the fixed molar ratio of $Ni_{0.8}Co_{0.1}Mn_{0.1}(OH)_2$:$Li_2SO_4$:LiOH is set as 4:1:6, the optimal calcination temperature is confirmed to be 900 °C.

Furthermore, the ratio of LiOH and Li_2SO_4 was determined (Table S1 in the ESM). In Fig. S6 in the ESM, the single crystalline particles size increases as LiOH proportion increases. According to ICP results (Table S3 in the ESM), the elemental composition of the obtained single crystal particles is consistent with $LiNi_{0.8}Co_{0.1}Mn_{0.1}O_2$ basically, indicating that the synthesis method is successful and effective. When *R* ($R = n(LiOH)/n(Li_2SO_4)$) reaches 6.0, the value of $I(003)/I(104)$ is the highest and the Li^+/Ni^{2+} mixing degree is the lowest as shown in Fig. S7 and Table S4 in the ESM. Therefore, the best synthesis condition is confirmed as bellow: the LiOH-Li_2SO_4 eutectic-salt system, preheat temperature of 500 °C, calcination temperature of 900 °C, and the *R* value of 6.0.

In order to explore the formation mechanism of single crystalline materials, a series of comparative experiments are carried out. The precursor mixed with different molten salts was calcined at 900 °C and its corresponding SEM images are shown in Fig. S8 in the ESM. It can be concluded that Li_2SO_4 promotes the dispersion of primary particles, while LiOH molten salt promotes uniform growth of primary particles. When heated to 900 °C, the precursor in LiOH-Li_2SO_4 eutectic-salt system can obtain dispersed and uniform single crystalline particles preferentially because of the lower eutectic point. Moreover, as shown in Fig. S9 in the ESM, the uniform primary particles cannot be obtained when the calcination temperature is not high enough or the heating time is too short, indicating that sufficiently high temperature and enough calcination time are required for the uniform growth of single crystalline particles. However, when the calcination temperature and time are fixed, as the proportion of LiOH in the system increases, the primary particles gradually change from octahedral to plate shapes (Fig. S6 in the ESM), indicating that the ratio of LiOH and Li_2SO_4 molten salt controls the morphology of single crystalline particles.

In general, the growth of single crystalline particles is guided by temperature, heating time, type, and proportion of molten salt. the change of particle morphology during a whole single crystalline growth process is observed by SEM, thus a schematic diagram of single crystalline growth path can be inferred as Fig. 2(a). When the temperature is lower than 800 °C, the particle morphology is similar to the precursor, which is agglomerated secondary particles; when the temperature rises to 800 °C, the secondary particles break and the primary particles start to grow; when the temperature reaches 900 °C, the disperse primary particles can be obtained. As the heating time extends, the primary particles gradually grow into single crystalline particles with a relatively regular and uniform morphology. In addition, when the agglomerated secondary particles disperse into primary particles, the primary particles will have different growth directions in different molten salt, which demonstrates that the morphology and dispersion degree of single crystalline particles are controlled

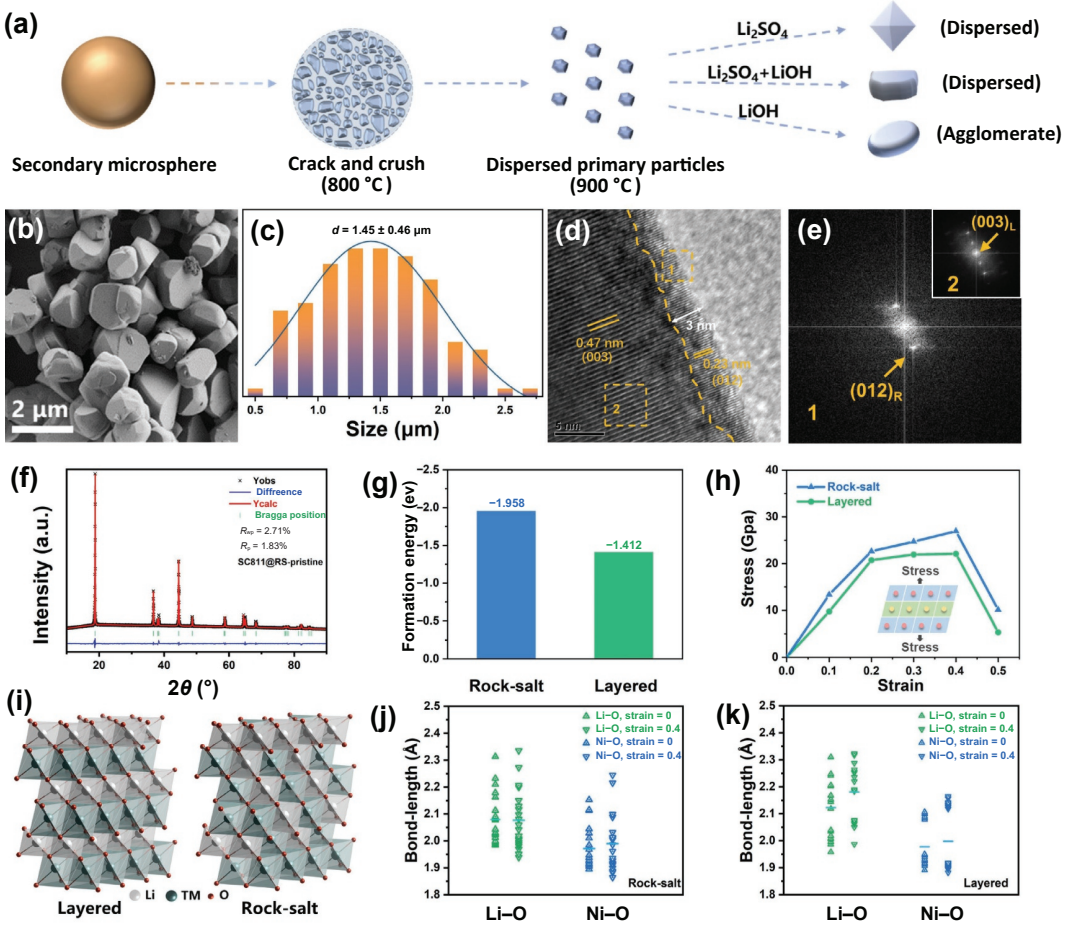

Figure 2 (a) Schematic illustration of the formation mechanism of single crystalline materials. (b) SEM image of SC811@RS. (c) Size distribution of SC811@RS particles. (d) HR-TEM image of SC811@RS. (e) FFT images and (f) XRD pattern and the Rietveld refinement results for pristine SC811@RS. (g) Formation energies of two structures. (h) Stress–strain curve for layered and rock-salt structures. (i) Schematic illustration of structures of SC811@RS material surface and bulk region. Bond-length distribution of Li–O and Ni–O in (j) rock-salt and (k) layered structures when the applied tensile strain is 0 and 0.4; the average value is shown in the bold line.

by the molten salt, and the presence of $SO4^{2-}$ can effectively prevent particle agglomeration.

The structure of SC811@RS obtained under the optimal synthesis conditions is investigated by SEM, high-resolution transmission electron microscopy (HR-TEM), and XRD. As shown in Figs. 2(b) and 2(c), SC811@RS materials are uniform single crystalline particles with the average size of 1–2 μm. The XRD result confirms that all patterns of the material can be indexed to the hexagonal α-$NaFeO_2$ structure with the $R\bar{3}m$ space group without any impurity phase, indicating the successful preparation of SC811@RS material (Fig. 2(f)). The Rietveld refinement result reveals that the SC811@RS material has a lower percentage of Li/Ni cation mixing (0.46%) than PC811 material (0.71%) (Tables S5 and S6, and Fig. S10 in the ESM). Additionally, the image of HR-TEM shows that the bulk region of SC811@RS particle is layered structure with a crystal interplanar spacing of 0.47 nm (Fig. 2(d)), which corresponds to the $R\bar{3}m$ space group. According to the fast Fourier transform (FFT) result (Fig. 2(e)) of material bulk region, it can be further confirmed that the bulk phase of SC811@RS material has a layered structure. Besides, the surface rock-salt structure layer with a thickness of 2–3 nm is constructed through washing and re-heating during the synthesis process of SC811@RS. As reported in the literature, the formation of the surface rock-salt phase may be due to the extraction of lattice lithium during the washing processes and migration of nickel ions in the material surface region [26, 34]. Figure S11 in the ESM shows the thermogravimetric analysis-mass spectrometry (TGA-MS) results for SC811@RS and PC811 samples. The most mass loss of SC811@RS started at 250 °C, which was higher than that of PC811 at 200 °C. It means that the thermal stability of SC811@RS material is better than PC811 material. And the delayed oxygen release of SC811@RS material may be due to the lower percentage of Li/Ni cation mixing [35].

To gain insight into effect of surface rock-salt structure layer on SC811@RS material, DFT calculation is used to evaluate the property difference between layered and rock-salt structure. The surface rock-salt structure layer is a thermodynamically stabilized interface as its formation energy is much lower than that of layered structure (Fig. 2(g)). In addition, we apply tensile stress on the structures in [003] direction to investigate their mechanical properties. As shown in Fig. 2(h), rock-salt structure can cope with stress easier, which means rock-salt structure can withstand a higher stress and has strengthened mechanical property. As reported in literature, when the tensile stress is applied to the layered structure in [003] direction, the bond-length of Li–O is stretched notably while that of NiO barely changes, indicating the delamination of structure is originated from Li layer and the Li–O bonds paly an major role in structural fracture behavior [36]. Due to the high binding capacity of Ni–O bond, the Ni^{2+} ions migrated to Li layer can be used as "anchor" to stabilize layered structure so that alleviating the deformation of structure. When the strain is 0.4 (the fracture critical point of structure), the average value of Li–O bond-length in rock-salt structure is significantly decreased compared with layered structure (Figs. 2(j) and 2(k)), indicating that the rock-salt structure can enhance the stability of material.

Electrochemical performances of SC811@RS and PC811 are investigated in the region of 3.0–4.3 V at 25 °C. Figure S12 in the ESM shows the first-cycle voltage profile of the SC811@RS and

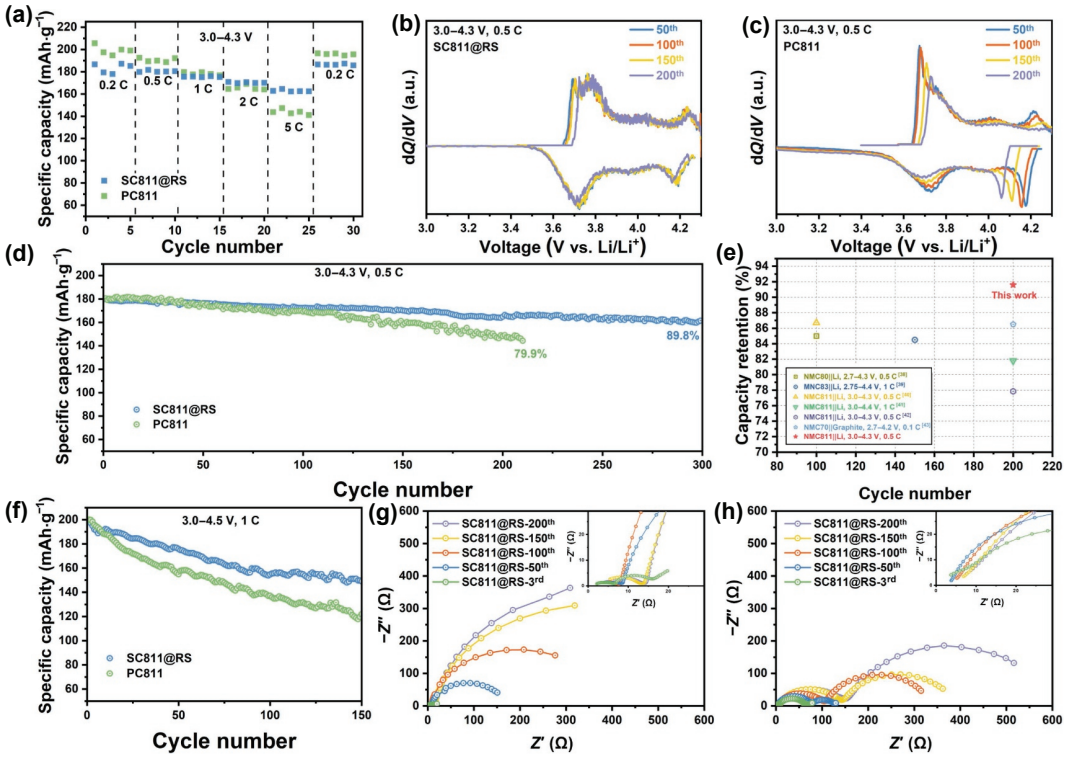

Figure 3 Electrochemical performance comparison of SC811@RS and PC811 electrode (a) Rate-capability tests of S811 and PC811 electrode. The differential capacity curves of (b) SC811@RS and (c) PC811 in the region of 3.0–4.3 V for 200 cycles. Cycling performance at 1 C in the voltage region of (d) 3.0–4.3 V and (f) 3.0–4.5 V, respectively. (e) The comparison between the Ni-rich cathode batteries and this work in terms of capacity retention and cycle life [38–43]. The EIS profiles of (g) SC811@RS and (h) PC811 electrode at charging potential.

PC811 electrodes at 0.5 C (1 C = 170 mAh·g^{-1}). SC811@RS displays an similar initial discharge capacity to that of PC811. However, the SC811@RS cathode showed better rate performance over the PC811 electrode as shown in Fig. 3(a). This may be due to the higher Li^+ diffusion rate of SC811@RS than PC811, as indicated by the GITT test in Fig. S13 in the ESM. Figures 3(b) and 3(c) exhibit the differential capacity curves of SC811@RS and PC811 at 3.0–4.3 V. The redox peaks in the region of 3.7–3.9 V are associated with the transformation of H1 phase to M phase [37]. However, the potential difference between the oxidation and reduction peaks of PC811 is larger than that of SC811@RS at the same cycle number, indicating PC811 has a larger electrode polarization and worse reversibility. The charging/discharging curves at selected cycle numbers are displayed in the Fig. S14 in the ESM. Similarly, in Fig. 3(d), the SC811@RS cathode shows a higher capacity of 163 mAh·g^{-1} and a better capacity retention rate of 92% after 200 cycles, than those of PC811 cathode (143 mAh·g^{-1} and 82%). The SC811@RS cathode also has a better cycle performance than PC811 under the high voltage region of 3.0–4.5 V, displaying a capacity retention of 75% after 150 cycles (Fig. 3(f)). Moreover, the interfacial charge transfer resistance R_{ct} of PC811 increased from 10.5 to 882.9 Ω after 200 cycles, which is much higher than that of SC811@RS (from 31.1 to 454.8 Ω), as shown in the Figs. 3(g) and 3(h), and Figure S15 and Table S7 in the ESM. According to the above results, it can be inferred that the electrochemical performance of SC811@RS is much better than that of PC811.

3.2 Capacity deterioration mechanism of SC811@RS and PC811

The possible reasons for differences in the electrochemical properties between SC811@RS and PC811 materials are also explored. The XRD patterns of cycled SC811@RS and PC811 electrodes are shown in Fig. 4. The peak positions in the XRD patterns are corrected with the $(220)_{Al}$ peak at 65.186°. All of the electrodes show a typical rhombohedral layered structure and a clear splitting of the (108)/(110) peaks, which means the material basically maintains a layered structure during cycle process [37, 44]. However, the (003) and (108) peaks of cycled material shift to a lower angle, which is reported to origin from the increase of *c*-axis due to the insufficient intercalation of Li^+ [42]. When the Ni ions occupy the Li ion sites, the transmission of Li ions is hindered and Li ions cannot reinsert into the structure sufficiently after cycles, leading to the capacity loss of electrode. After 200 cycles, the (003) peak angle deviation of PC811 material (0.16°) is larger than that of SC811@RS material (0.14°) and the lattice distortion rate of material is the same trend (0.83% for PC811 and 0.72% for SC811@RS), which indicates a better structural reversibility of SC811@RS during cycle process, corresponding to superior electrochemical performance.

In order to further analyze the reasons for differences in the structure reversibility of material after cycling, the morphology changes of SC811@RS and PC811 electrodes before and after cycling are observed by SEM. As shown in the Fig. S16 in the ESM, there have no apparent microcracks in SC811@RS materials before and after 200 cycles. However, a few microcracks appear on the surface of the PC811 electrode after 50 cycles and more cracks appear after 200 cycles. From the cross section of particles, the phenomenon is more obvious (Figs. 4(c)–4(f)). Similarly, the morphology of the SC811@RS particles remains intact after 200 cycles, while the PC811 particles crack obviously and some large gaps are exposed. The existence of internal microcracks in the particles not only causes part of materials to lose electrical contact but also allows the electrolyte to penetrate into the particles easily and aggravates the side reactions between the electrolyte and the material [45]. Therefore, the suppression of microcracks in the particles ensures the good structural reversibility of SC811@RS during the cycle, which is consistent with the XRD results.

The surface structural evolution of cycle SC811@RS and PC811 samples is revealed by TEM measurements. As shown in the TEM

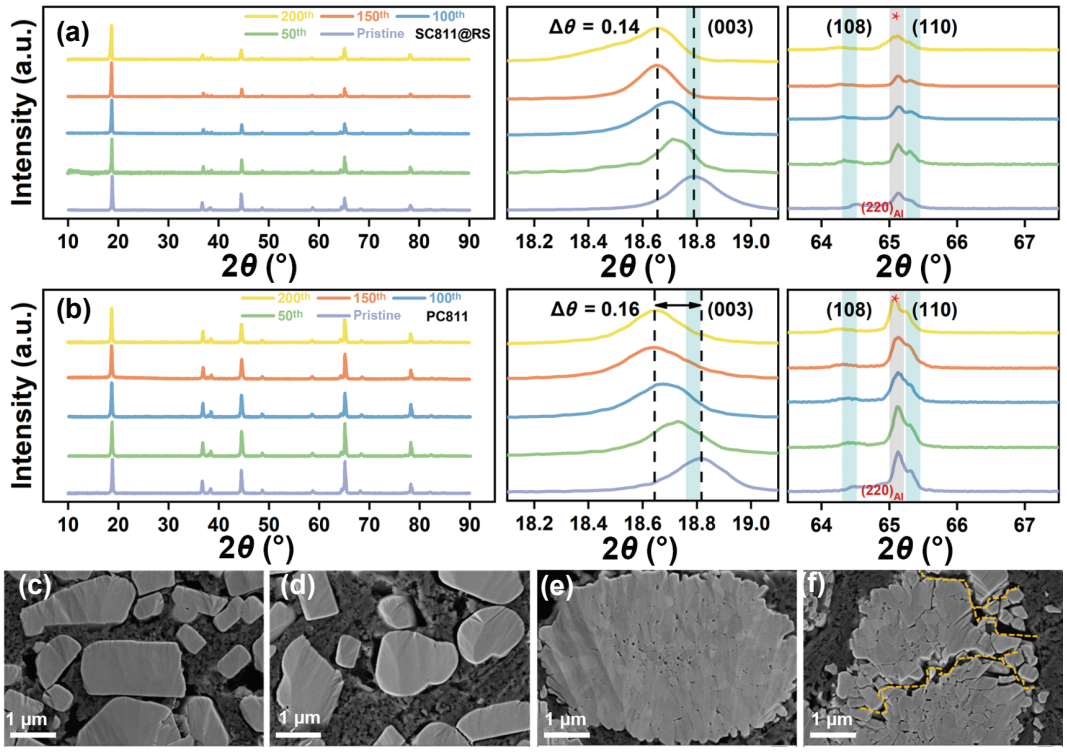

Figure 4 XRD patterns of (a) SC811@RS and (b) PC811 electrodes after selected cycles. Cross-sectional SEM images of the SC811@RS electrode collected after (c) 50 and (d) 200 cycles. Cross-sectional SEM images of the PC811 electrode surface collected after (e) 50 and (f) 200 cycles.

and the FFT images, the bulk regions of both the pristine SC811@RS and PC811 materials show a consistent layered structure (Figs. 5(f) and 5(g)). But there is a thermodynamically stabilized interface (rock-salt structure) with the thickness of 2–3 nm on the surface of SC811@RS material along the lithium ion deintercalation direction (Fig. 5(f), region 1). After 200 cycles at a region of 3.0–4.3 V (Figs. 5(h) and 5(i)), the thickness of the rock-salt passivation layer on the surface of SC811@RS particles hardly increases (Fig. 5(h), region 4). In contrast, that of PC811 particles (17 nm) increases significantly (Fig. 5(i), region 6). It indicates that the thermodynamically stabilized interface of the SC811@RS-pristine material lessens the side reaction between the electrode material and the electrolyte, and inhibits the further surface structure deterioration of SC811@RS during the cycling [46]. However, during the cycle, the severe surface structure deterioration of the PC811 material hinders the insertion and extraction of lithium ions, resulting in the deteriorative structure reversibility of material, which is also consistent with the XRD characterization results. Through XPS we further analyze surface species changes during the cycle. The Ni 2p spectrum has two major peaks at 854.8 and 856.8 eV corresponding to Ni^{2+} and Ni^{3+}, respectively [47]. From the Ni 2p spectra, the ratio of Ni^{2+} for SC811@RS-pristine sample is slightly higher than that of PC811-pristine sample due to the presence of the thermodynamically stabilized interface of SC811@RS material (Figs. 5(a) and 5(b)). After 200 cycles, the content of Ni^{3+} on the surface of SC811@RS slightly drops from 64.6% to 64.3%, while part of Ni^{2+} transform into NiF_2 and the content of NiF_2 increases to 35.4% (Figs. 5(c) and 5(e)). In comparison, the content of Ni^{3+} on the surface of PC811 drops significantly (41.5%) and the content of Ni^{2+} (13.5%)/NiF_2 (45.0%) increases (Figs. 5(d) and 5(e)). In addition, the XPS analyses of C, O, and F elements are shown in Fig. S17 in the ESM. Those prove that the side reactions occur at the electrode/electrolyte interface and the side reactions of the PC811 material are more serious, which is consistent with the TEM results [48].

In summary, it is believed that SC811@RS material can maintain good structural reversibility during long cycle, thus exhibiting a better electrochemical performance than PC811 material, which is mainly due to the suppression of internal micro-cracks and surface structure deterioration in the SC811@RS material.

Furthermore, the difference in structure reversibility of SC811@RS and PC811 during long-term cycles is compared from multiple scales by Raman spectroscopy. The previous work of our research group shows that the Ni-rich NCM material has two Raman active modes (A_{1g} and E_g), which are attributed to stretching vibration of M–O (M = Ni, Co, and Mn) bond and bending vibration of O–M–O bond, respectively. The A_{1g} and E_g vibrational modes can be further deconvolved into four Raman active modes: A_{1g} (Ni, Co) ≈ 550 cm^{-1}, A_{1g} (Mn) ≈ 610 cm^{-1}, E_g (Ni, Co) ≈ 476 cm^{-1}, and E_g (Mn) ≈ 595 cm^{-1} [49]. The redox reaction of Ni^{2+}/Ni^{4+} causes changes of MO_6 local coordination structure, resulting in the variation of peak intensity. In Fig. 6(a), the Raman spectra of SC811@RS basically coincide after cycling 3, 50, and 200 cycles, indicating a good structural reversibility of SC811@RS during long-term cycles. The focused ion beam technique is used to split the cycled SC811@RS and PC811 materials to expose their cross-sections. Whether the Raman spectra between different SC811@RS particles at different electrode depths (Fig. 6(b), and Figs. S18(a) and S18(c) in the ESM) or those between the surface and bulk regions of the same SC811@RS particle (Fig. 6(c)), are almost the same during cycling. This further confirms the excellent structural reversibility and reaction homogeneity of SC811@RS at the particle, electrode, and time scales. Noting that the Raman spectral difference between the pristine and cycled SC811@RS may be related to the low coulombic efficiency of the first cycle [50].

For the PC811 material, the A_{1g} (Ni, Co) peak and E_g (Ni, Co) peak intensities of the different particles after 200 cycles generally increase compared to the E_g (Mn) peak intensity (Fig. 6(d)), indicating that the reduction depth of PC811 material decreases, and the irreversibility of the layered structure increases after 200 cycles [37, 51]. It is worth noting that the Raman peak differs

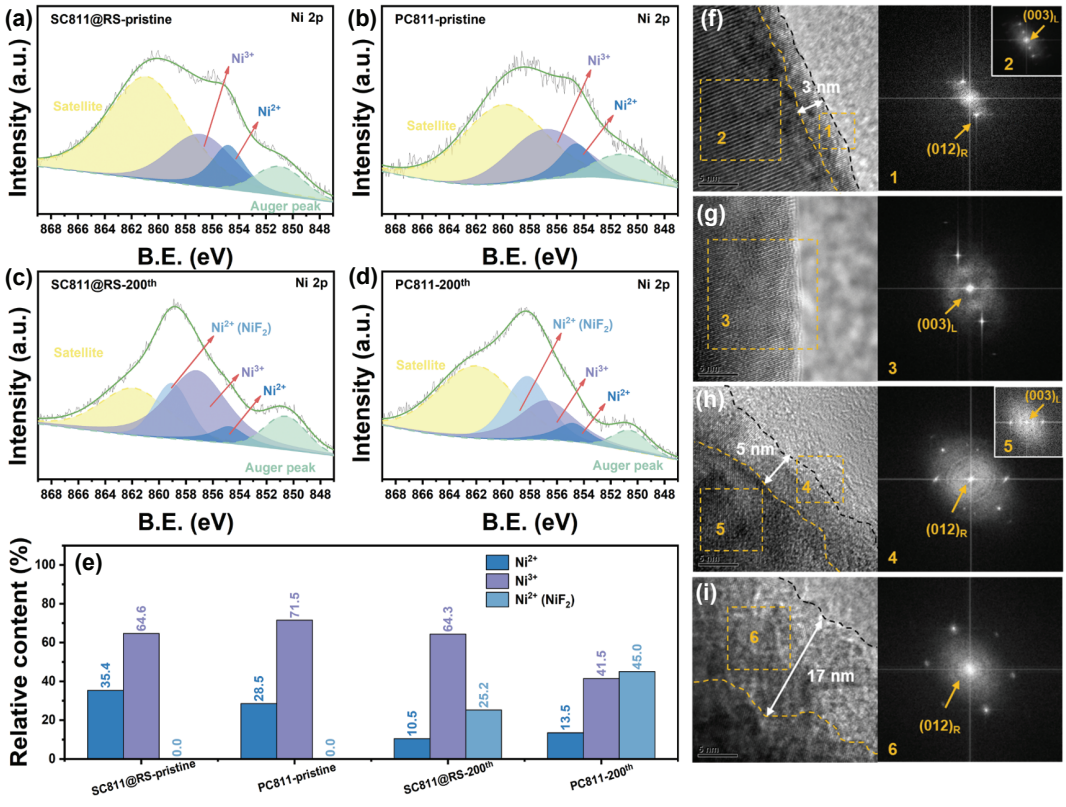

Figure 5 The XPS spectra of Ni 2p for (a) the pristine SC811@RS sample, (b) the pristine PC811 sample, (c) the SC811@RS sample, and (d) the PC811 sample in the region of 3.0–4.3 V for 200 cycles. (e) The relative contents of Ni^{2+}, NiF_2, and Ni^{3+} on the electrode surface before and after cycle. HR-TEM images and corresponding FFT for (f) the pristine SC811@RS sample, (g) the pristine PC811 sample, (h) the SC811@RS sample, and (i) the PC811 sample in the region of 3.0–4.3 V for 200 cycles.

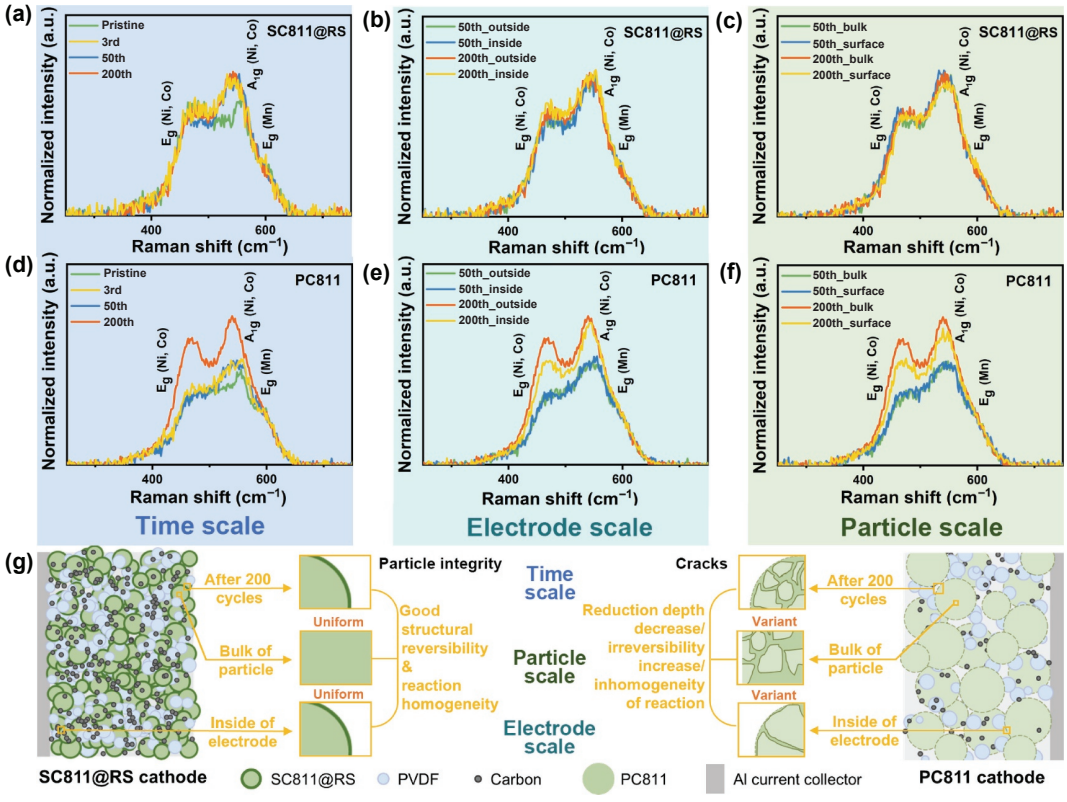

Figure 6 Raman spectra of ((a)–(c)) SC811@RS electrode and ((d)–(f)) PC811 electrode and (g) schematic diagram of SC811@RS and PC811 structural reversibility difference during long-term cycles.

greatly after 200 cycles whether it is particles at different electrode depths (Fig. 6(e), and Figs. S18(b) and S18(d) in the ESM), or the bulk and surface regions of the same particles (Fig. 6(f)). It is reported that the particles near the surface of electrode have a higher availability compared with the particles inside the electrode during charging and discharging process [52]. They are broken easily, which causes the bulk structure of the particle to lose electrical contact and affects its structural reversibility. This shows

the poor structural reversibility and reaction homogeneity of PC811 at the particle, electrode, and time scales.

Based on the above results, the superior electrochemical performance of SC811@RS material can be ascribed to bulk structure integrity without microcracks, which can inhibit the spread of side reactions along the grain boundaries. Besides, the thermodynamically stabilized interface on the surface of the pristine SC811@RS material lessens the side reaction between the electrode material and the electrolyte, and mitigates further surface structure deterioration. The above reasons ensure good structural reversibility and reaction uniformity of SC811@RS material during cycles，thus possess a better electrochemical performance compared with PC811 material.

4 Conclusions

In this work, the SC811@RS is successfully prepared by the molten-salt method. The morphological evolution of single crystalline material growth path is observed by SEM and the possible growth mechanism of single crystalline particles is inferred. Compared with the PC811 electrode, the cycle stability of SC811@RS electrode has been significantly improved, and the cycle retention at 1 C rate was 86% after 200 cycles. The main cause for the capacity decay of PC811 electrode is the deterioration of structural reversibility and reaction uniformity. Single crystalline particles significantly inhibit the generation of microcracks in the particles, lessen the parasitic reactions, and mitigate further surface structure deterioration. Those characteristics enhance the stability of cathode which increases the cycle life of batteries.

Acknowledgements

We gratefully acknowledge the financial support of the Key Project of Science and Technology of Xiamen (No. 3502Z20201013) and the National Natural Science Foundation of China (Nos. 21875198, 21875195, and 22021001). We also acknowledge the help of Tan Kah Kee Innovation Laboratory on the scientific tests.

Electronic Supplementary Material: Supplementary material (XRD patterns, TG-MS curves, optical images, SEM images, electrochemical tests, and flow chart) is available in the online version of this article at https://doi.org/10.1007/s12274-022-4768-6.

References

[1] Mizushima, K.; Jones, P. C.; Wiseman, P. J.; Goodenough, J. B. Li_xCoO_2 ($0 < x < -1$): A new cathode material for batteries of high energy density. *Mater. Res. Bull.* **1980**, *15*, 783–789.

[2] Megahed, S.; Scrosati, B. Lithium-ion rechargeable batteries. *J. Power Sources* **1994**, *51*, 79–104.

[3] Manthiram, A. An outlook on lithium ion battery technology. *ACS Cent. Sci.* **2017**, *3*, 1063–1069.

[4] Li, W. D.; Erickson, E. M.; Manthiram, A. High-nickel layered oxide cathodes for lithium-based automotive batteries. *Nat. Energy* **2020**, *5*, 26–34.

[5] Kempton, W. Electric vehicles: Driving range. *Nat. Commun.* **2016**, *1*, 16131.

[6] Schmuch, R.; Wagner, R.; Hörpel, G.; Placke, T.; Winter, M. Performance and cost of materials for lithium-based rechargeable automotive batteries. *Nat. Commun.* **2018**, *3*, 267–278.

[7] Su, X.; Wu, Q. L.; Li, J. C.; Xiao, X. C.; Lott, A.; Lu, W. Q.; Sheldon, B. W.; Wu, J. Silicon-based nanomaterials for lithium-ion batteries: A review. *Adv. Energy Mater.* **2014**, *4*, 1300882.

[8] Yin, S. Y.; Deng, W. T.; Chen, J.; Gao, X.; Zou, G. Q.; Hou, H. S.; Ji, X. B. Fundamental and solutions of microcrack in Ni-rich layered oxide cathode materials of lithium-ion batteries. *Nano Energy* **2021**, *83*, 105854.

[9] Manthiram, A.; Song, B. H.; Li, W. D. A perspective on nickel-rich layered oxide cathodes for lithium-ion batteries. *Energy Storage Mater.* **2017**, *6*, 125–139.

[10] Chen, R. S.; Li, Q. H.; Yu, X. Q.; Chen, L. Q.; Li, H. Approaching practically accessible solid-state batteries: Stability issues related to solid electrolytes and interfaces. *Chem. Rev.* **2020**, *120*, 6820–6877.

[11] Noh, H. J.; Youn, S.; Yoon, C. S.; Sun, Y. K. Comparison of the structural and electrochemical properties of layered $Li[Ni_xCo_yMn_z]O_2$ (x = 1/3, 0.5, 0.6, 0.7, 0.8 and 0.85) cathode material for lithium-ion batteries. *J. Power Sources* **2013**, *233*, 121–130.

[12] Zou, L. F.; Zhao, W. G.; Jia, H. P.; Zheng, J. M.; Li, L. Z.; Abraham, D. P.; Chen, G. Y.; Croy, J. R.; Zhang, J. G.; Wang, C. M. The role of secondary particle structures in surface phase transitions of Ni-rich cathodes. *Chem. Mater.* **2020**, *32*, 2884–2892.

[13] Zhang, S.; Ma, J.; Hu, Z. L.; Cui, G. L.; Chen, L. Q. Identifying and addressing critical challenges of high-voltage layered ternary oxide cathode materials. *Chem. Mater.* **2019**, *31*, 6033–6065.

[14] Xie, Q.; Li, W. D.; Manthiram, A. A Mg-doped high-nickel layered oxide cathode enabling safer, high-energy-density Li-ion batteries. *Chem. Mater.* **2019**, *31*, 938–946.

[15] Han, B. H.; Key, B.; Lapidus, S. H.; Garcia, J. C.; Iddir, H.; Vaughey, J. T.; Dogan, F. From coating to dopant: How the transition metal composition affects alumina coatings on Ni-rich cathodes. *ACS Appl. Mater. Interfaces* **2017**, *9*, 41291–41302.

[16] Bianchini, M.; Roca-Ayats, M.; Hartmann, P.; Brezesinski, T.; Janek, J. There and back again-the journey of $LiNiO_2$ as a cathode active material. *Angew. Chem., Int. Ed.* **2019**, *58*, 10434–10458.

[17] Yang, H. P.; Wu, H. H.; Ge, M. Y.; Li, L. J.; Yuan, Y. F.; Yao, Q.; Chen, J.; Xia, L. F.; Zheng, J. M.; Chen, Z. Y. et al. Simultaneously dual modification of Ni-rich layered oxide cathode for high-energy lithium-ion batteries. *Adv. Funct. Mater.* **2019**, *29*, 1808825.

[18] Gao, S.; Zhan, X. W.; Cheng, Y. T. Structural, electrochemical and Li-ion transport properties of Zr-modified $LiNi_{0.8}Co_{0.1}Mn_{0.1}O_2$ positive electrode materials for Li-ion batteries. *J. Power Sources* **2019**, *410–411*, 45–52.

[19] Liu, W.; Li, X. F.; Hao, Y. C.; Xiong, D. B.; Shan, H.; Wang, J. J.; Xiao, W.; Yang, H. J.; Yang, H.; Kou, L. et al. Functional passivation interface of $LiNi_{0.8}Co_{0.1}Mn_{0.1}O_2$ toward superior lithium storage. *Adv. Funct. Mater.* **2021**, *31*, 2008301.

[20] Zhang, C. F.; Zhao, W. G.; Zheng, S. Y.; Li, Y. X.; Gong, Z. L.; Zhang, Z. R.; Yang, Y. Research progresses in Ni-Co-Mn/Al ternary concentration gradient cathode materials for Li-ion batteries. *J. Electrochem.* **2020**, *26*, 73–83.

[21] Kim, J.; Lee, H.; Cha, H.; Yoon, M.; Park, M.; Cho, J. Prospect and reality of Ni-rich cathode for commercialization. *Adv. Energy Mater.* **2018**, *8*, 1702028.

[22] Li, J.; Li, H. Y.; Stone, W.; Weber, R.; Hy, S.; Dahn, J. R. Synthesis of single crystal $LiNi_{0.5}Mn_{0.3}Co_{0.2}O_2$ for lithium ion batteries. *J. Electrochem. Soc.* **2017**, *164*, A3529–A3537.

[23] Langdon, J.; Manthiram, A. A perspective on single-crystal layered oxide cathodes for lithium-ion batteries. *Energy Storage Mater.* **2021**, *37*, 143–160.

[24] Kim, Y. Lithium nickel cobalt manganese oxide synthesized using alkali chloride flux: Morphology and performance As a cathode material for lithium ion batteries. *ACS Appl. Mater. Interfaces* **2012**, *4*, 2329–2333.

[25] Tu, W. Q.; Wang, X. S.; Tian, W. Y.; Zhou, Y. N.; Han, C. P.; Li, C.; Kang, F. Y.; Li, B. H. A green water-induced spinel heterostructure interface enabling high performance lithium and manganese rich oxides. *J. Mater. Chem. A* **2021**, *9*, 20576–20584.

[26] Zhang, Q. Q.; Liu, K.; Li, C.; Li, L.; Liu, X. J.; Li, W.; Zhang, J. L. *In situ* induced surface reconstruction of single-crystal lithium-ion cathode toward effective interface compatibility. *ACS Appl. Mater. Interfaces* **2021**, *13*, 13771–13780.

[27] Wu, F.; Li, N.; Su, Y. F.; Shou, H. F.; Bao, L. Y.; Yang, W.; Zhang, L. J.; An, R.; Chen, S. Spinel/layered heterostructured cathode material for high-capacity and high-rate Li-ion batteries. *Adv. Mater.* **2013**, *25*, 3722–3726.

[28] Kresse, G.; Furthmüller, J. Efficient iterative schemes for *ab initio*

total-energy calculations using a plane-wave basis set. *Phys. Rev. B* **1996**, *54*, 11169–11186.
[29] Perdew, J. P.; Burke, K.; Ernzerhof, M. Generalized gradient approximation made simple. *Phys. Rev. Lett.* **1996**, *77*, 3865–3868.
[30] Kresse, G.; Joubert, D. From ultrasoft pseudopotentials to the projector augmented-wave method. *Phys. Rev. B* **1999**, *59*, 1758–1775.
[31] Blöchl, P. E. Projector augmented-wave method. *Phys. Rev. B* **1994**, *50*, 17953–17979.
[32] Grimme, S.; Antony, J.; Ehrlich, S.; Krieg, H. A consistent and accurate *ab initio* parametrization of density functional dispersion correction (DFT-D) for the 94 elements H-Pu. *J. Chem. Phys.* **2010**, *132*, 154104.
[33] *LiOH-Li_2SO_4 Phase Diagram* [Online]. https://www.crct.polymtl.ca/fact/phase_diagram.php?file=LiOH-Li2SO4.jpg&dir=FTsalt (accessed Aug 7, 2021).
[34] Park, J. H.; Choi, B.; Kang, Y. S.; Park, S. Y.; Yun, D. J.; Park, I.; Shim, J. H.; Park, J. H.; Han, H. N.; Park, K. Effect of residual lithium rearrangement on Ni-rich layered oxide cathodes for lithium-ion batteries. *Energy Technol.* **2018**, *6*, 1361–1369.
[35] Sharifi-Asl, S.; Lu, J.; Amine, K.; Shahbazian-Yassar, R. Oxygen release degradation in Li-ion battery cathode materials: Mechanisms and mitigating approaches. *Adv. Energy Mater.* **2019**, *9*, 1900551.
[36] Min, K.; Cho, E. Intrinsic origin of intra-granular cracking in Ni-rich layered oxide cathode materials. *Phys. Chem. Chem. Phys.* **2018**, *20*, 9045–9052.
[37] Li, J. Y.; Huang, J. X.; Li, H. Y.; Kong, X. B.; Li, X.; Zhao, J. B. Insight into the redox reaction heterogeneity within secondary particles of nickel-rich layered cathode materials. *ACS Appl. Mater. Interfaces* **2021**, *13*, 27074–27084.
[38] Ryu, H. H.; Namkoong, B.; Kim, J. H.; Belharouak, I.; Yoon, C. S.; Sun, Y. K. Capacity fading mechanisms in Ni-rich single-crystal NCM cathodes. *ACS Energy Lett.* **2021**, *6*, 2726–2734.
[39] Fan, X. M.; Hu, G. R.; Zhang, B.; Ou, X.; Zhang, J. F.; Zhao, W. G.; Jia, H. P.; Zou, L. F.; Li, P.; Yang, Y. Crack-free single-crystalline Ni-rich layered NCM cathode enable superior cycling performance of lithium-ion batteries. *Nano Energy* **2020**, *70*, 104450.
[40] Zou, Y. G.; Mao, H. C.; Meng, X. H.; Du, Y. H.; Sheng, H.; Yu, X. Q.; Shi, J. L.; Guo, Y. G. Mitigating the kinetic hindrance of single-crystalline Ni-rich cathode via surface gradient penetration of tantalum. *Angew. Chem., Int. Ed.* **2021**, *60*, 26535–26539.
[41] Zhu, J.; Zheng, J. C.; Cao, G. L.; Li, Y. J.; Zhou, Y.; Deng, S. Y.; Hai, C. X. Flux-free synthesis of single-crystal $LiNi_{0.8}Co_{0.1}Mn_{0.1}O_2$ boosts its electrochemical performance in lithium batteries. *J. Power Sources* **2020**, *464*, 228207.
[42] Kong, X. B.; Zhang, Y. G.; Peng, S. Y.; Zeng, J.; Zhao, J. B. Superiority of single-crystal to polycrystalline $LiNi_xCo_yMn_{1-x-y}O_2$ cathode materials in storage behaviors for lithium-ion batteries. *ACS Sustainable Chem. Eng.* **2020**, *8*, 14938–14948.
[43] Bi, Y. J.; Tao, J. H.; Wu, Y. Q.; Li, L. Z.; Xu, Y. B.; Hu, E. Y.; Wu, B. B.; Hu, J. T.; Wang, C. M.; Zhang, J. G. et al. Reversible planar gliding and microcracking in a single-crystalline Ni-rich cathode. *Science* **2020**, *370*, 1313–1317.
[44] Kong, X. B.; Peng, S. Y.; Li, J. Y.; Chen, Z. J.; Chen, Z. Q.; Wang, J.; Zhao, J. B. Pre-blended conductive agent to effectively improve the storage properties of $LiNi_{0.6}Co_{0.2}Mn_{0.2}O_2$ cathode materials. *J. Power Sources* **2020**, *448*, 227445.
[45] Li, W. D.; Song, B. H.; Manthiram, A. High-voltage positive electrode materials for lithium-ion batteries. *Chem. Soc. Rev.* **2017**, *46*, 3006–3059.
[46] Lin, R. Q.; Bak, S. M.; Shin, Y.; Zhang, R.; Wang, C. Y.; Kisslinger, K.; Ge, M. Y.; Huang, X. J.; Shadike, Z.; Pattammattel, A. et al. Hierarchical nickel valence gradient stabilizes high-nickel content layered cathode materials. *Nat. Commun.* **2021**, *12*, 2350.
[47] Chen, Z.; Wang, J.; Chao, D. L.; Baikie, T.; Bai, L. Y.; Chen, S.; Zhao, Y. L.; Sum, T. C.; Lin, J. Y.; Shen, Z. X. Hierarchical porous $LiNi_{1/3}Co_{1/3}Mn_{1/3}O_2$ nano-/micro spherical cathode material: Minimized cation mixing and improved Li^+ mobility for enhanced electrochemical performance. *Sci. Rep.* **2016**, *6*, 25771.
[48] Li, J. Y.; Huang, J. X.; Kong, X. B.; Zeng, J.; Zhao, J. B. The apparent capacity decay by kinetic degradation of $LiNi_{0.5}Co_{0.2}Mn_{0.3}O_2$ during cycling under the high upper-limit charging potential. *J. Power Sources* **2021**, *496*, 229856.
[49] Li, J. Y.; Hua, H. M.; Kong, X. B.; Yang, H. Y.; Dai, P. P.; Zeng, J.; Zhao, J. B. *In-situ* probing the near-surface structural thermal stability of high-nickel layered cathode materials. *Adv. Energy Mater.* **2022**, *46*, 90–99.
[50] Kasnatscheew, J.; Evertz, M.; Streipert, B.; Wagner, R.; Klöpsch, R.; Vortmann, B.; Hahn, H.; Nowak, S.; Amereller, M.; Gentschev, A. C. et al. The truth about the 1st cycle coulombic efficiency of $LiNi_{1/3}Co_{1/3}Mn_{1/3}O_2$ (NCM) cathodes. *Phys. Chem. Chem. Phys.* **2016**, *18*, 3956–3965.
[51] Ghanty, C.; Markovsky, B.; Erickson, E. M.; Talianker, M.; Haik, O.; Tal-Yossef, Y.; Mor, A.; Aurbach, D.; Lampert, J.; Volkov, A. et al. Li^+-ion extraction/insertion of Ni-rich $Li_{1+x}(Ni_yCo_zMn_z)_wO_2$ ($0.005 < x < 0.03$; $y{:}z = 8{:}1$, $w \approx 1$) electrodes: *In situ* XRD and Raman spectroscopy study. *ChemElectroChem* **2015**, *2*, 1479–1486.
[52] Cha, H.; Kim, J.; Lee, H.; Kim, N.; Hwang, J.; Sung, J.; Yoon, M.; Kim, K.; Cho, J. Boosting reaction homogeneity in high-energy lithium-ion battery cathode materials. *Adv. Mater.* **2020**, *32*, 2003040.